Constrained Predictive Control Based on a Large-Signal Model for a Three-Phase Inverter Connected to a Microgrid

Carlos Alfaro, Ramon Guzman, Member,*IEEE*, Luis Garcia de Vicuña, Jaume Miret, Member,*IEEE*, Miguel Castilla

***Abstract*—Small-signal models are the mostly used to model and design in inverter-dominated microgrids. Conversely, this paper proposes a large-signal model for grid-forming inverters connected to a microgrid based on the active and reactive power dynamic equations. In this work, it is proposed to use this nonlinear model to develop a constrained predictive control for the inverters connected to a microgrid. The main features of this proposed control are: first, direct voltage control (in amplitude and frequency) is not necessary; second, stability is guaranteed under a wide range of line impedances (hence, the virtual impedance is not needed); and third, the proposed control can operate with unbalanced and nonlinear loads. Moreover, a theoretical stability analysis is presented. Selected experimental results show that the proposed control operates satisfactorily in case of a load step change, a load imbalance, and nonlinear loads.**

***Index Terms*—AC Microgrid, large-signal model, model predictive control, inverter.**

I. Introduction

NOWADAYS, microgrids are becoming an interesting research field due to their capability of integrating different kind of energy resources. A microgrid is conceived as a cluster of distributed generation (DG) systems which can operate in both grid connected or islanded modes [1].

In islanded microgrids based on voltage source inverters (VSIs), the control system is responsible for regulating the frequency and amplitude of the microgrid voltage. A hierarchical control architecture is widely used which is divided into three control layers [2]–[5]. The primary layer is responsible for controlling active and reactive power. The active power is usually controlled in a decentralized manner, i.e., without using communication network and ensuring stability following the grid codes. The secondary layer purpose is to correct the steady-state deviation introduced by the primary layer. The secondary control can be decentralised, centralised or distributed. Finally, the tertiary control is usually responsible for controlling the energy dispatching.

Focusing on the primary layer, the droop control has been used during the past in power sharing [6]–[10]. This method has been widely accepted by researches for microgrids applications due to its advantages [11], [12]. However, there are some limitations for power sharing in the conventional droop control since it depends of the line impedance [5]. Moreover, to achieve a better power sharing, some distributed droop-inspired controllers are presented in the literature [13]–[15], where communications are required. Nevertheless, the controllers based on the droop method assume a purely inductive or resistive line impedance. This assumption decouples the active and reactive power controls. The microgrid impedance may change when a load or source is connected or disconnected. Therefore, the power sharing accuracy decreases and the microgrid may become unstable [16]. An accurate power sharing using the droop method has been also presented in the past with the use of a virtual impedance in lines with a high resistance/inductance (R/X) ratio [17]. However, virtual impedance uses the output current as a feedforward term to generate the voltage references. Thus, in presence of unbalanced or nonlinear loads, the virtual impedance will provoke distorted voltage reference that will result in unbalanced three-phase voltages. To avoid these effects of the virtual impedance, in [18] an adaptive droop control is proposed. In this approach, a novel adaptive control is designed to achieve the stability of microgrid under varying network configuration. The drawbacks of this method are that the active power sharing accuracy is reduced, and the microgrid frequency presents steady-state deviation. Moreover, the reactive power sharing is not considered.

In the droop control, the dynamics of the microgrid system is obtained by using static equations for active and reactive powers [19]–[21]. The mathematical models normally used are small-signals models and the system dynamics can be only described in a small neighborhood around the equilibrium point. Therefore, large variations cannot be accurately captured by the small-signal models, since they cannot predict these kind of behaviors [4].

With the development of digital signal processors (DSP) the model predictive control (MPC) has attracted more and more attention. This technique has become a promising control

Manuscript received November 13, 2020; revised February 15, 2021 and May 20, 2021; accepted July 2, 2021.

This work was supported by the Ministry of Science, Innovation and Universities of Spain and by the European Regional Development Fund under project RTI2018-100732-B-C22.

Carlos Alfaro, Luis Garcia de Vicuña, Jaume Miret and Miguel Castilla are with the Department of Electronic and Electrical Engineering, Technical University of Catalonia, 08800 Vilanova i la Geltru, Spain (e-mail: carlos.arturo.alfaro@upc.edu; vicuna@eel.upc.edu; jmiret@eel.upc.edu; miquel.castilla@upc.edu).

Ramon Guzman is with the Department of Automatic control, Technical University of Catalonia, 08800 Vilanova i la Geltru, Spain (e-mail: ramon.guzman@upc.edu).

method with advantages such as fast transient response, high control bandwidth, and providing a simple way to include nonlinearities and constraints [22]–[32]. In [24]–[29] the MPC is applied to the inner loops, i.e., the current and voltage controllers, of the inverters connected to aa AC microgrid. Moreover, the power sharing control is based on the droop method on theses proposals. Besides, in [30]–[32] the MPC is applied to the secondary control and the droop method is used as primary control. However, they inevitably inherit some of the droop control drawbacks presented above.

In the MPC, the control algorithm is based on the prediction of the state variables using a discrete model. In regards to this technique, a cost function is minimized inside a predictive window to obtain the vector of future control actions. Moreover, the optimal design of MPC based on the system parameters is used in this paper to achieve an accurate power-sharing, in addition to being robust against a wide range of line impedance.

The contributions of this paper are a novel large-signal model for grid-forming inverters operating in a microgrid, and the controller design methodology using the MPC. The use of the MPC will allow to include constraints in the voltages amplitude providing an excellent voltage regulation. The main advantages can be summarized as follows:

1) A more accurate dynamic description of the system is achieved, which is not only useful to know the exact system dynamics but also allows to design new control proposals.
2) Robustness against line impedance variations, hence the virtual impedance is not needed.
3) The controller operates satisfactorily in case of unbalanced and nonlinear loads, providing balanced three-phase voltages and reducing the voltage THD. Compared with the traditional droop method, this is an important improvement.
4) The voltage amplitude of the inverter can be regulated by applying constraints to the cost function of the MPC.
5) The frequency and voltage restoration are not necessary.

This paper is organized as follows. In section II a large-signal model of the inverter is presented. Section III deals with the proposed control system. The stability analysis is presented in section IV while in section V the experimental results are reported. Finally, section VI draws some conclusions of this proposal.

II. Large-signal model of the inverter

Fig.1 depicts the equivalent circuit of a single three-phase inverter connected to an AC microgrid. This inverter is modelled by an AC voltage source defined by $E\angle\phi$ which is connected to a bus where its voltage is $V\angle 0$ through a RL line impedance. Note that i is the current flowing from the inverter to the grid.

In the $\alpha\beta$ frame, the equations of the active and reactive power supplied by the inverter can be expressed as follows:

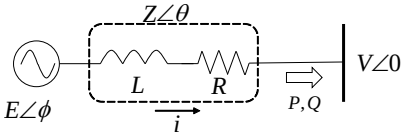

Fig. 1. Equivalent circuit of the inverter

$$P = \frac{3}{2}\left(v_\alpha i_\alpha + v_\beta i_\beta\right) \tag{1}$$

$$Q = \frac{3}{2}\left(v_\beta i_\alpha - v_\alpha i_\beta\right). \tag{2}$$

Besides, from Fig.1, the differential equations for the inverter output current i are:

$$\frac{di_\alpha}{dt} = \frac{1}{L}\left(e_\alpha - i_\alpha R - v_\alpha\right) \tag{3}$$

$$\frac{di_\beta}{dt} = \frac{1}{L}\left(e_\beta - i_\beta R - v_\beta\right). \tag{4}$$

The dynamic equations of the active and reactive powers can be obtained by taking the first time derivative of (1)-(2), yielding:

$$\frac{dP}{dt} = \frac{3}{2}\left(v_\alpha\frac{di_\alpha}{dt} + i_\alpha\frac{dv_\alpha}{dt} + v_\beta\frac{di_\beta}{dt} + i_\beta\frac{dv_\beta}{dt}\right) \tag{5}$$

$$\frac{dQ}{dt} = \frac{3}{2}\left(v_\beta\frac{di_\alpha}{dt} + i_\alpha\frac{dv_\beta}{dt} - v_\alpha\frac{di_\beta}{dt} - i_\beta\frac{dv_\alpha}{dt}\right). \tag{6}$$

In the aforementioned equations it is usual to define $e_\alpha = Esin(\omega t + \phi)$, $e_\beta = -Ecos(\omega t + \phi)$, $v_\alpha = Vsin(\omega t)$ and $v_\beta = -Vcos(\omega t)$, being ω the grid frequency. According to these definitions the following relations can be found:

$$\frac{dv_\alpha}{dt} = -\omega v_\beta \tag{7}$$

$$\frac{dv_\beta}{dt} = \omega v_\alpha. \tag{8}$$

Using (3)-(4) and (7)-(8) in (5) and (6), the dynamic equations of the active and reactive powers delivered by the inverter to the microgrid can be rewritten as follows:

$$\frac{dP}{dt} = \frac{3}{2L}\left(-V^2 + EVcos(\phi)\right) - \frac{R}{L}P - \omega Q \tag{9}$$

$$\frac{dQ}{dt} = -\frac{3}{2L}EVsin(\phi) - \frac{R}{L}Q + \omega P. \tag{10}$$

Note that the well-known steady-state equations of P and Q can be easily obtained from the point of equilibrium, making (9) and (10) equal to zero, respectively

$$P = \frac{3}{2}\frac{V}{Z}\left[(Ecos(\phi) - V)cos(\theta) + Esin(\theta)sin(\phi)\right] \tag{11}$$

$$Q = \frac{3}{2}\frac{V}{Z}\left[(Ecos(\phi) - V)sin(\theta) - Ecos(\theta)sin(\phi)\right] \tag{12}$$

where Z and θ are the magnitude and phase values of the output and line impedance.

Expressions (11) and (12) have been traditionally obtained by analyzing the circuit of Fig.1. In the previous works, the controller design has been performed according to the

static expressions of P and Q, (11)-(12) [19]. Unlike other works, the novelty in this paper is that the controller can be derived using the dynamic equations (9) and (10). Note that the dynamic model (9) and (10) is clearly non-linear. However, considering that the bus voltage is a slow variable, thus V can be considered constant. In addition, by defining the control signals vector as $\mathbf{u} = [u_1 \;\; u_2]$, the following change of variables, that linearizes (9) and (10), can be obtained:

$$u_1 = Ecos(\phi) \tag{13}$$

$$u_2 = Esin(\phi) \tag{14}$$

or equivalently

$$E = \sqrt{u_1^2 + u_2^2} \tag{15}$$

$$\phi = \arctan(u_1/u_2). \tag{16}$$

With these considerations (9) and (10) can be rewritten as a linear large-signal model:

$$\frac{dP}{dt} = \frac{3}{2L}\left(-V^2 + Vu_1\right) - \frac{R}{L}P - \omega Q \tag{17}$$

$$\frac{dQ}{dt} = -\frac{3}{2L}Vu_2 - \frac{R}{L}Q + \omega P. \tag{18}$$

III. Proposed Control System

This section presents the proposed control system. The main objective is to regulate the active and reactive powers to achieve accurate power sharing. The controller is based on an MPC where a cost function is used to minimize the error between the active and reactive powers and their references. Besides, a constraint on the control signal u_1 is imposed to regulate the voltage amplitude E, usually between $\pm 5\%$ of its nominal value, below the allowed tolerance [33].

A. State-Space Model with Embedded Integrator

An incremental model of the inverter is presented in this section. The proposed model is represented by a multiple input and multiple output (MIMO) system. If (17)-(18) are expressed as a state-space model, it gives:

$$\begin{pmatrix} \frac{dP}{dt} \\ \frac{dQ}{dt} \end{pmatrix} = \begin{pmatrix} -\frac{R}{L} & -\omega \\ \omega & -\frac{R}{L} \end{pmatrix} \begin{pmatrix} P \\ Q \end{pmatrix} + \begin{pmatrix} \frac{3V}{2L} & 0 \\ 0 & -\frac{3V}{2L} \end{pmatrix} \begin{pmatrix} u_1 \\ u_2 \end{pmatrix} + \begin{pmatrix} -\frac{3}{2L} \\ 0 \end{pmatrix} V^2. \tag{19}$$

The aforementioned model is discretized using the Euler first order approximation, as follows:

$$\mathbf{x}_m(k+1) = \mathbf{A}_m\mathbf{x}_m(k) + \mathbf{B}_m\mathbf{u}(k) + \mathbf{D}_m d(k) \tag{20}$$

$$\mathbf{y}(k) = \mathbf{C}_m\mathbf{x}_m(k) \tag{21}$$

where $\mathbf{x}_m = [P \;\; Q]^T$ is the state-space vector, $\mathbf{u} = [u_1 \;\; u_2]^T$ is the control signals vector, $d(k) = V^2$ is considered as a disturbance and the matrices $\mathbf{A}_m$, $\mathbf{B}_m$ $\mathbf{C}_m$ and $\mathbf{D}_m$ are defined as

$$\mathbf{A}_m = \begin{pmatrix} 1 - \frac{T_s R}{L} & -\omega T_s \\ \omega T_s & 1 - \frac{T_s R}{L} \end{pmatrix}; \mathbf{C}_m = \begin{pmatrix} 1 & 0 \\ 0 & 1 \end{pmatrix}$$

$$\mathbf{B}_m = \begin{pmatrix} \frac{3T_s V}{2L} & 0 \\ 0 & -\frac{3T_s V}{2L} \end{pmatrix}; \mathbf{D}_m = \begin{pmatrix} -\frac{3T_s V^2}{2L} \\ 0 \end{pmatrix}$$

where T_s is the sample time.

Now, in order to eliminate the steady-state error and the effect of the uncertainties, an integrator is embedded in the model. If the difference operation is applied to (20), an incremental model is obtained

$$\begin{aligned} \mathbf{x}_m(k+1) - \mathbf{x}_m(k) &= \mathbf{A}_m(\mathbf{x}_m(k) - \mathbf{x}_m(k-1)) \\ &+ \mathbf{B}_m(\mathbf{u}(k) - \mathbf{u}(k-1)) + \mathbf{D}_m(d(k) - d(k-1)) \end{aligned} \tag{22}$$

or equivalently

$$\begin{aligned} \Delta\mathbf{x}_m(k+1) &= \mathbf{A}_m\Delta\mathbf{x}_m(k) + \mathbf{B}_m\Delta\mathbf{u}(k) \\ &+ \mathbf{D}_m\Delta d(k) \end{aligned} \tag{23}$$

where $\Delta\mathbf{x}_m$, $\Delta\mathbf{u}$ and Δd are the incremental variables of the state, the control signals and the disturbance vectors, respectively. It is worth to mention that since $d(k) = V^2$ is practically a constant voltage in a sampling period, $\Delta d(k) = d(k) - d(k-1) \simeq 0$. This approximation allows to eliminate the disturbance term from the incremental model.

In a similar way, the incremental output vector is expressed as:

$$\mathbf{y}(k+1) - \mathbf{y}(k) = \mathbf{C}_m(\mathbf{x}_m(k+1) - \mathbf{x}_m(k)). \tag{24}$$

From (23) and (24), a new augmented state-space model can be defined which contains the incremental state variables and the output vector $\mathbf{y}$:

$$\mathbf{x}(k+1) = \mathbf{A}\mathbf{x}(k) + \mathbf{B}\Delta\mathbf{u}(k) \tag{25}$$

$$\mathbf{y}(k) = \mathbf{C}\mathbf{x}(k) \tag{26}$$

being $\mathbf{x}(k) = [\Delta\mathbf{x}_m(k) \;\; \mathbf{y}(k)]^T$ and the matrices of the augmented model are obtained from $\mathbf{A}_m$, $\mathbf{B}_m$, $\mathbf{C}_m$ and $\mathbf{D}_m$ as:

$$\mathbf{A} = \begin{pmatrix} \mathbf{A}_m & \mathbf{0}_{2\times 2} \\ \mathbf{C}_m\mathbf{A}_m & \mathbf{I}_{2\times 2} \end{pmatrix}; \mathbf{C} = \begin{pmatrix} \mathbf{0}_{2\times 2} & \mathbf{I}_{2\times 2} \end{pmatrix}$$

$$\mathbf{B} = \begin{pmatrix} \mathbf{B}_m \\ \mathbf{C}_m\mathbf{B}_m \end{pmatrix}; \mathbf{D} = \begin{pmatrix} \mathbf{D}_m \\ \mathbf{C}_m\mathbf{D}_m \end{pmatrix}$$

where matrix $\mathbf{I}_{2\times 2}$ is the identity matrix and $\mathbf{0}_{2\times 2}$ a square matrix of zeros.

B. Cost Function

As it was stated, the control objective is to achieve power sharing by regulating the active and reactive powers. The cost function which reflects the control objectives can be defined as follows [22]:

$$\mathbf{J} = ||(\mathbf{Y}^* - \mathbf{Y})||^2 + \Delta\mathbf{U}^T\mathbf{R}\Delta\mathbf{U} \tag{27}$$

where $\mathbf{R} = r_\omega\mathbf{I}_{2N_c\times 2N_c}$ is a diagonal matrix of dimension N_c where N_c is defined as the control horizon, $r_\omega > 0$ is the control effort used as a tuning parameter to adjust a desired closed loop performance and $\mathbf{Y}^*$ is the reference vector which can be expressed in the following form:

$$\mathbf{Y}^* = [\underbrace{\mathbf{I}_{2\times 2} \;\; \mathbf{I}_{2\times 2} \;\; \dots \;\; \mathbf{I}_{2\times 2}}_{N_p}]\mathbf{r}(k_i) = \bar{\mathbf{R}}\mathbf{r}(k_i). \tag{28}$$

Note that $\mathbf{r}(k_i) = [P^*(k_i) \;\; Q^*(k_i)]$ is the reference vector at the sampling instant k_i, and the size of $\mathbf{Y}^*$ is the optimization window also called the prediction horizon, N_p.

On the other hand, the future control trajectory is denoted by the vector $\Delta\mathbf{U}$ as:

$$\Delta\mathbf{U} = \left[\Delta\mathbf{u}(k_i)^T \;\; \dots \;\; \Delta\mathbf{u}(k_i + N_c - 1)^T\right]^T \tag{29}$$

which size is N_c.

The future outputs are contained in the vector $\mathbf{Y}$, which is defined as follows

$$\mathbf{Y} = \left[\; \mathbf{y}(k_i + 1|k_i)^T \;\; \cdots \;\; \mathbf{y}(k_i + N_p|k_i)^T \;\right]^T \tag{30}$$

where it can be expressed as a function of the current state variables and the future control trajectory [23]:

$$\mathbf{Y} = \mathbf{F}\mathbf{x}(k_i) + \mathbf{G}\Delta\mathbf{U}. \tag{31}$$

In the last equation, $\mathbf{F}$ is a vector of dimension N_p and $\mathbf{G}$ is a matrix of dimension $N_c \times N_p$, respectively

$$\mathbf{F} = \left(\; \mathbf{CA} \;\; \mathbf{CA}^2 \;\; \cdots \;\; \mathbf{CA}^{N_p} \;\right)^T \tag{32}$$

$$\mathbf{G} = \begin{pmatrix} \mathbf{CB} & \mathbf{0}_{2\times2} & \cdots & \mathbf{0}_{2\times2} \\ \mathbf{CAB} & \mathbf{CB} & \cdots & \mathbf{0}_{2\times2} \\ \vdots & \vdots & \ddots & \vdots \\ \mathbf{CA}^{N_p-1}\mathbf{B} & \mathbf{CA}^{N_p-2}\mathbf{B} & \cdots & \mathbf{CA}^{N_p-N_c}\mathbf{B} \end{pmatrix} \tag{33}$$

C. Cost Function Minimization with Constraints

In this section, the minimization of a constrained cost function for the MIMO system is presented. With this objective in mind, the cost function presented in (27) is rewritten using (31) in (27), leading to

$$\mathbf{J} = \Delta\mathbf{U}^T\mathbf{\Phi}\Delta\mathbf{U} + \Delta\mathbf{U}^T\mathbf{H} + ||(\mathbf{Y}^* - \mathbf{F}\mathbf{x})||^2 \tag{34}$$

where

$$\mathbf{\Phi} = \mathbf{G}^T\mathbf{G} + \mathbf{R} \tag{35}$$

$$\mathbf{H} = -2\mathbf{G}^T(\mathbf{Y}^* - \mathbf{F}\mathbf{x}). \tag{36}$$

Looking at the equation (13) it is observed that for a small value of ϕ, the control signal u_1 can be approximated to the voltage amplitude E, $u_1 \approx E$. Then to achieve a minimization of the cost function (34) adding a constraint in u_1 is equivalent to minimize (34) with a constraint in the voltage amplitude E. With this idea, the voltage of the inverter can be regulated in a small range near to its nominal value. Then, according to (29) it holds that:

$$u_1(k_i) = u_1(k_i - 1) + \Delta u_1(k_i) \tag{37}$$

and considering the approximation $u_1 \approx E$, the following inequality constraints are formulated:

$$E_{min} \leq u_1(k_i) \leq E_{max}. \tag{38}$$

The aforementioned expression can be rewritten as a function of the incremental control vector if (37) is used in (38), yielding

$$E_{min} \leq u_1(k_i - 1) + \mathbf{C}_1\Delta\mathbf{U}\mathbf{C}_2 \leq E_{max} \tag{39}$$

where $\mathbf{C}_1$ and $\mathbf{C}_2$ corresponds to the appropriate matrices which in this case are defined as follows:

$$\mathbf{C}_1 = \underbrace{\begin{pmatrix} 1 & 0 & 0 & 0 & \dots & 0 \\ 0 & 0 & 0 & 0 & \dots & 0 \end{pmatrix}}_{N_c}; \mathbf{C}_2 = (1 \;\; 0)^T.$$

Then, to formulate the constrained MPC problem, equation (39) is rewritten as two inequalities constraints:

$$-\mathbf{C}_1\Delta\mathbf{U} \leq [-E_{min} + u_1(k_i - 1)]\mathbf{C}_2^T \tag{40}$$

$$\mathbf{C}_1\Delta\mathbf{U} \leq [E_{max} - u_1(k_i - 1)]\mathbf{C}_2^T. \tag{41}$$

Taking into account that the term $||(\mathbf{Y}^* - \mathbf{F}\mathbf{x})||^2$ in (34) does not depend on the control vector $\Delta\mathbf{u}$, the optimization problem with the inequality constraints is formulated as follows:

$$\frac{\partial}{\partial\Delta\mathbf{U}}(\Delta\mathbf{U}^T\mathbf{\Phi}\Delta\mathbf{U} + \Delta\mathbf{U}^T\mathbf{H}) = 0 \tag{42}$$

subject to:

$$0 \leq \gamma \tag{43}$$

$$\gamma = \begin{pmatrix} [-E_{min} + u_1(k_i - 1)]\,\mathbf{C}_2^T \\ [E_{max} - u_1(k_i - 1)]\,\mathbf{C}_2^T \end{pmatrix} - \mathbf{M}\Delta\mathbf{U}. \tag{44}$$

where $\mathbf{M} = (-\mathbf{C}_1 \;\; \mathbf{C}_1)^T$.

The solution of the aforementioned equations leads to the optimum control signal vector which accomplishes the constraints in the component $u_1(k_i)$ or equivalently in the voltage amplitude $\mathbf{E}$, and it is expressed as follows:

$$\Delta\mathbf{U} = -\mathbf{\Phi}^{-1}(\mathbf{H} + \mathbf{M}^T\lambda) \tag{45}$$

where λ is a vector containing the zero or positive values of the Lagrange multipliers. Note that $\Delta\mathbf{U}$ can be separated into two different terms, $\mathbf{\Phi}^{-1}\mathbf{H}$ and $\mathbf{\Phi}^{-1}\mathbf{M}^T\lambda$. The first term is the optimum solution without any constraint while the second term accounts for the constraints. This optimization problem can be solved using the Hildreth's quadratic programming [22].

Based on the receding horizon principle, the actual control signals $\Delta\mathbf{u}(k_i) = [\Delta u_1(k_i) \;\; \Delta u_2(k_i)]^T$ can be obtained as:

$$\Delta\mathbf{u}(k_i) = -\mathbf{W}\mathbf{\Phi}^{-1}(\mathbf{H} + \mathbf{M}^T\lambda) \tag{46}$$

with

$$\mathbf{W} = [\underbrace{\mathbf{I}_{2\times2} \;\; \mathbf{0}_{2\times2} \;\; \dots \;\; \mathbf{0}_{2\times2}}_{N_c}]$$

and the control signal is generated by adding the incremental value to the last value $\mathbf{u}(k_i - 1)$

$$\mathbf{u}(k_i) = \mathbf{u}(k_i - 1) + \Delta\mathbf{u}(k_i). \tag{47}$$

D. Controller Implementation

In this section the proposed controller implementation is presented. To reduce the computational burden the solution

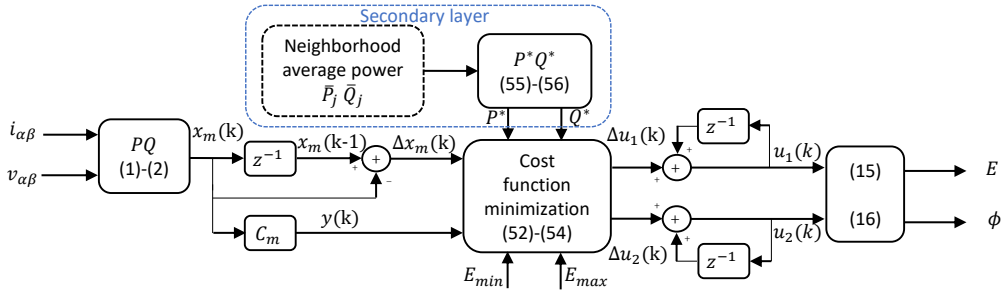

Fig. 2. Block diagram of the proposed MPC

of the cost function minimization (46) can be rewritten using (35) and (36):

$$\begin{aligned}\Delta\mathbf{u}(k_i) &= \mathbf{K}_r\mathbf{r}(k_i) - \mathbf{K}_c\mathbf{x}(k_i) - \mathbf{K}_\lambda\lambda \\ &= \mathbf{K}_r(\mathbf{r}(k_i) - \mathbf{y}(k_i)) - \mathbf{K}_x\Delta\mathbf{x}_m(k_i) - \mathbf{K}_\lambda\lambda\end{aligned} \tag{48}$$

where

$$\mathbf{K}_r = \mathbf{W}(\mathbf{G}\mathbf{G}^T + \mathbf{R})\mathbf{G}^T\bar{\mathbf{R}} \tag{49}$$

$$\mathbf{K}_c = \mathbf{W}(\mathbf{G}\mathbf{G}^T + \mathbf{R})\mathbf{G}^T\mathbf{F} \tag{50}$$

$$\mathbf{K}_\lambda = \mathbf{W}\mathbf{\Phi}^{-1}\mathbf{M}^T. \tag{51}$$

Note that $\mathbf{K}_c = [\mathbf{K}_x \;\; \mathbf{K}_r]$ is the gain of the MPC controller, and does not depend on the Lagrange multipliers. According to the last expression, it holds that

$$\Delta\mathbf{u}(k_i) = -\mathbf{K}_c\tilde{\mathbf{x}}(k_i) - \mathbf{K}_\lambda\lambda \tag{52}$$

where

$$\tilde{\mathbf{x}}(k_i) = [\Delta\mathbf{x}_m(k_i) \;\; \mathbf{y}(k_i) - \mathbf{r}(k_i)]^T. \tag{53}$$

It should be noted that the term $-\mathbf{K}_c\tilde{\mathbf{x}}(k_i)$ may be implemented as easy as a full state feedback controller, and the gains $\mathbf{K}_c$ and $\mathbf{K}_\lambda$ are obtained offline.

Typically, λ is calculated online using the Hildreth's quadratic programming. It is worth noting that λ converges to the set of λ^*, where λ^* contains zeros in the inactive constraints and positive value in the active constraint $\lambda^*_{\mathbf{act}}$. However, since the active constraint can be correctly identified from (40) or (41) in each sample period, the converged $\lambda^*_{\mathbf{act}}$ can be defined as follows [22]:

$$\lambda^*_{\mathbf{act}} = -(\mathbf{M}_{act}\mathbf{\Phi}^{-1}\mathbf{M}^T_{act})^{-1}\gamma_{\mathbf{act}} \tag{54}$$

where $\gamma_{\mathbf{act}}$ correspond to the active constrain and $(\mathbf{M}_{act}\mathbf{\Phi}^{-1}\mathbf{M}^T_{act})^{-1}$ is calculated offline for each constrain as follows:

$$\mathbf{M}_{act} = \begin{cases} C_{act} & if \quad 0 \leq -E_{min} + u_1(k_i - 1) + \Delta u_1(k) \\ -C_{act} & if \quad 0 \leq E_{max} - u_1(k_i - 1) - \Delta u_1(k) \end{cases}$$

$$C_{act} = \underbrace{\begin{pmatrix} 1 & 0 & 0 & 0 & \dots & 0 \end{pmatrix}}_{N_c}$$

Fig. 2 shows the block diagram of the proposed MPC algorithm. As shown in the figure, the control signals are obtained by the solution of the cost function minimization (52)-(54). The inputs to the controller are the local inverter voltage and current measures, the minimum and maximum values of the voltage amplitude, E_{min} and E_{max}, and the neighborhood inverters average powers, $\bar{P}_j$ and $\bar{Q}_j$, received among a communication network. The power references are calculated from the neighborhood inverters average powers, as follows:

$$P^* = \sum_{j=1}^{n_i} \frac{a_{ij}\bar{P}_j}{n_i} \tag{55}$$

$$Q^* = \sum_{j=1}^{n_i} \frac{a_{ij}\bar{Q}_j}{n_i} \tag{56}$$

where the coefficients a_{ij} determine the availability of communication between inverters i and j, thus indicating the set of nodes n_i that exchange control data including the local inverter. Thus, $a_{ij} = a_{ji} = 1$ if nodes i and j can exchange their data, otherwise $a_{ij} = a_{ji} = 0$. Besides $a_{ii} = 1$.

As shown in Fig. 2, the inverter voltage and current measures are used to calculate the local instantaneous active and reactive power measures, P and Q, that are used to generate the vector $\mathbf{x}(k)$. This vector allows obtaining the new space-state vector $\mathbf{x}(k)$, formed by $\Delta\mathbf{x}_m(k)$ and the output $\mathbf{y}(k)$. Since the proposed control uses an incremental model with a embedded integrator (25)-(26), the incremental control signals are calculated based on (52)-(54), and the control signal is generated by adding the incremental value to the last value $\mathbf{u}(k_i - 1)$. Hence, using (47) the control signals vector, $u_1(k)$ and $u_2(k)$, are obtained as $u_1(k) = u_1(k-1) + \Delta u_1(k)$ and $u_2(k) = u_2(k-1) + \Delta u_2(k)$, respectively. Then, the voltage amplitude and phase angle setpoint are calculated based on the nonlinear transformation defined in (15) and (16).

Finally, once the voltage amplitude and phase angle setpoint are computed, the inner loop is responsible to generate the voltage signals. The voltage set point used by the inner loop is expressed as follows:

$$e^* = Esin(\omega_o t + \phi). \tag{57}$$

IV. Closed-loop System

In this section, the closed-loop system is analyzed. For this purpose, from (52) and (53), the closed-loop equation may be written as follows:

$$\tilde{\mathbf{x}}(k_i + 1) = (\mathbf{A} - \mathbf{B}\mathbf{K}_c)\tilde{\mathbf{x}}(k_i) - \mathbf{B}\mathbf{K}_\lambda\lambda. \tag{58}$$

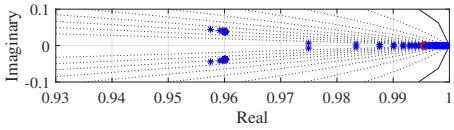

Fig. 3. Closed-loop poles for r_ω variation from 1×10^6 to 1×10^9.

TABLE I
SYSTEM PARAMETERS

Description	Symbol	Value
Microgrid voltage	V	110 V_{rms}
Microgrid frequency	f	60 Hz
Nominal dc-link voltage	V_{dc}	400 V
Line inductance model	L	10 mH
Line resistance model	R	2 Ω
Prediction horizon	N_p	80
Control horizon	N_c	20
Control effort	r_ω	1×10^8
Sampling frequency	f_s	10 kHz
Switching frequency	f_{sw}	10 kHz

Furthermore, if the constrained term $\mathbf{K}_\lambda \lambda$ is not considered for the stability analysis, the closed-loop eigenvalues can be obtained by solving the determinant

$$|\mathbf{A} - \mathbf{B}\mathbf{K}_c - \lambda \mathbf{I}| = 0 \tag{59}$$

The eigenvalues have a dependence of $\mathbf{K}_c$ and, as a consequence, of $\mathbf{R}$. As evidenced by the last expression, by selecting the appropriate value of $\mathbf{R}$, a desired dynamics of the MPC can be obtained.

The proposed MPC parameters are designed according to a dynamics specification using the closed-loop eigenvalues (59) and the system parameters listed in table I. The design has been developed from the closed-loop poles as a function of the control effort parameter r_ω. The prediction and control horizons, N_p and N_c, has been selected as $N_{c,i}$ = 20 and $N_{p,i}$ = 80. Fig. 3 shows the position of the closed-loop poles for a control effort variation in the range $10^6 \leq r_\omega \leq 10^9$. The poles in red are the closed-loop poles for r_ω = 1×10^8, which is the selected value used in the experimental results. Besides, the selected pole deal with a theoretical settling time approximately 1.5 s.

Additionally, in order to analyze the stability under absence of communication network, from (55)-(56) the active and reactive power reference can be expressed as local variables (i.e. $P^* = P_i$ and $Q^* = Q_i$), hence $\mathbf{r}(k_i) = \mathbf{y}(k_i)$. Then, the embedded integrator is removed from (48). Besides, if the constrained term is not considered for the stability analysis, (48) can be rewritten as follows:

$$\Delta \mathbf{u}(k_i) = -\mathbf{K}_x \Delta \mathbf{x}_m(k_i) \tag{60}$$

or equivalently

$$\mathbf{u}(k_i) = -\mathbf{K}_x \mathbf{x}_m(k_i) \tag{61}$$

Finally, the closed-loop eigenvalues can be obtained by solving the determinant

$$|\mathbf{A_m} - \mathbf{B_m}\mathbf{K}_x - \lambda \mathbf{I}| = 0 \tag{62}$$

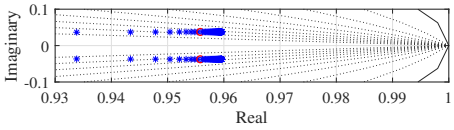

Fig. 4. Closed-loop poles under absence of communication network for r_ω variation from 1×10^6 to 1×10^9.

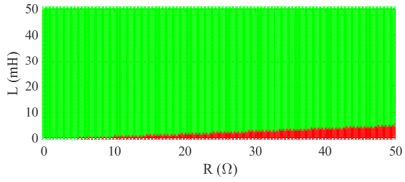

Fig. 5. Stability condition for 0.1 mH $< L <$ 50 mH and 0.1 Ω $< R <$ 50 Ω.

Fig. 4 shows the position of the closed-loop poles under absence of communication network for a control effort variation in the range $10^6 \leq r_\omega \leq 10^9$. As it can be seen, the stability is ensured for all values of the control effort.

V. Lyapunov-based stability analysis

This section deals with the stability analysis of the proposed controller. For this purpose, (58) may be rewritten as follows:

$$\tilde{\mathbf{x}}(k_i + 1) = (\tilde{\mathbf{A}} - \tilde{\mathbf{B}}\mathbf{K}_c)\tilde{\mathbf{x}}(k_i) - \tilde{\mathbf{B}}\mathbf{K}_\lambda \lambda \tag{63}$$

$$\tilde{\mathbf{A}} = \mathbf{A} + \Delta\mathbf{A}; \tilde{\mathbf{B}} = \mathbf{B} + \Delta\mathbf{B}$$

where A and B are the matrices of the nominal model, and $\Delta\mathbf{A}$ and $\Delta\mathbf{B}$ regards to the model uncertainties.

Considering the definition in (53), the cost function defined in (27) can be rewritten as a discrete-time linear quadratic regulator

$$\begin{aligned} J_{opt} = &\sum_{m=1}^{N_p} \tilde{\mathbf{x}}_{opt}^T(k_i + m|k_i)\tilde{\mathbf{x}}_{opt}(k_i + m|k_i) \\ &+ \sum_{m=0}^{N_c-1} \Delta\mathbf{u}_{opt}^T(k_i + m|k_i) r_\omega \Delta\mathbf{u}_{opt}(k_i + m|k_i). \end{aligned} \tag{64}$$

Since the last equation is quadratic, it can be used as a Lyapunov function for the stability analysis. Then, defining the Lyapunov candidate as [34]:

$$V(\tilde{\mathbf{x}}(k_i), k_i) = J_{opt} \tag{65}$$

and taking into account that in the classic MPC, the stability is achieved if the Lyapunov function decreases along the state trajectory, it can be written:

$$V(\tilde{\mathbf{x}}(k_i + 1), k_i + 1) - V(\tilde{\mathbf{x}}(k_i), k_i) < 0. \tag{66}$$

Using (52), (63), (65) and (66), the following condition is obtained

$$(\tilde{\mathbf{A}} - \tilde{\mathbf{B}}\mathbf{K}_c)^T(\tilde{\mathbf{A}} - \tilde{\mathbf{B}}\mathbf{K}_c) - \mathbf{K}_c^T r_\omega \mathbf{K}_c - \mathbf{I} < 0. \tag{67}$$

Fig. 6. Photograph of the experimental microgrid.

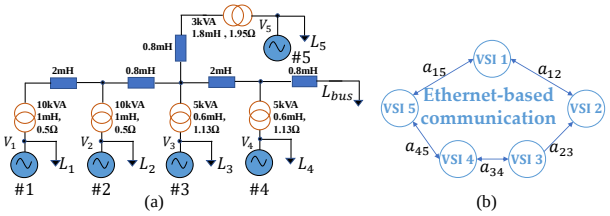

Fig. 7. Diagram of the laboratory microgrid setup: (a) electrical network and (b) communication network.

Equation (67) shows that the stability is affected by the parameter uncertainties and depends on $\mathbf{K}_c$, and as a consequence, on the parameters selection. To analyze the robustness of the proposed control under impedances uncertainties, the stability condition (67) is evaluated for different values of R and L. Thus, substituting $r_\omega = 1 \times 10^8$, $N_p = 80$ and $N_c = 20$ in (67) and sweeping L from 0.1 mH to 50 mH and R from 0.1 Ω to 50 Ω, the system presents stability for a wide range of impedances. Fig 5 shows the stability condition for a wide range of impendence. The green region shows the stable impedance range and the red region shows the unstable impedances range. As shown, for small values of L when R increase the system tends to instability. To conclude this section, the system is stable as long as the impedance angle $\theta > 0.04$ rads.

VI. Experimental Results

This section presents the experimental tests implemented in the laboratory microgrid shown in Fig. 6 and 7. On the one hand, in Fig. 7 (a) it is shown the electrical network. The microgrid is formed by five grid-forming inverters, each one with local loads that may be connected or disconnected. Each inverter was built using a 2.3-kVA Guasch MTL-CBI0060F12IXHF full bridge as the power converter and is driven by a 32-bit dual-core DSP Concerto-F28M36P63C, with a sampling frequency of 10 kHz. This device is composed of a C28 DSP core for control purposes and a Cortex M3 ARM for communications. Moreover, two three-phase balanced loads are considered to be connected to the microgrid each that may be connected or disconnected in the position shown in Fig. 7 (a) to form the global load L_{bus}. Moreover, in Table II the equivalent line impedance seen by each inverter is presented. From Table II, it should be noted that the inverter

TABLE II
EQUIVALENT LINE IMPEDANCE

Description	Value	(X/R) ratio
Impedances seen by VSI 1	$0.76 + 1.34j\ \Omega$	1.76
Impedances seen by VSI 2	$0.80 + 0.74j\ \Omega$	0.92
Impedances seen by VSI 3	$1.32 + 0.40j\ \Omega$	0.30
Impedances seen by VSI 4	$1.30 + 0.76j\ \Omega$	0.59
Impedances seen by VSI 5	$1.50 + 0.80j\ \Omega$	0.54

1 line impedance is mainly inductive while inverter 3, 4, and 5 line impedances are mainly resistive. In addition, the inverter 2 line impedance presents no dominant behavior. Taking all these impedances in mind, it is clear that the microgrid is operating in a mixed scenario with resistive, inductive and complex impedances. On the other hand, in Fig. 7 (b) it is shown the communication network. The microgrid uses the UDP Protocol over an Ethernet link to communicate the M3 cores with a transmission rate of 0.1 s. Finally, the circles represent the cyber nodes of the communication network, and the bidirectional arrows determine the availability of communication between inverters.

A. Performance Evaluation

To validate the performance of the novel MPC with the parameters shown in Table II, the following experimental test was designed in the laboratory setup. First, to validate the plug and play capability, the five VSIs are connected at different time, t =0, 10, 20, 30 and 40 s, respectively. In t =0 s the inverter 1 starts and fixes the microgrid frequency and voltage while feeds a balanced load connected in the bus, with a total power demand above 1.6 kW. The activation of the following inverters is done using a phase-locked loop for synchronizing them to the microgrid voltage phase. Besides, at time t =60 s the inverter 5 is disconnected. Finally, with the aim to analyze the performance of the microgrid under load change at t =50 s the second balanced load is connected.

Fig. 8 shows the active power by each inverter (Fig. 8 (a)), as well as their reactive powers (Fig. 8 (b)), their frequencies (Fig. 8 (c)), and the bus voltages (Fig. 8 (d)). As it can be observed in the Fig. 8 (a) and Fig. 8 (b) after each connection, the active and reactive power sharing is achieved. Moreover, Fig. 8 (c) shows that the microgrid frequency in steady state is the nominal, with only slight changes when an inverter or load is connected/disconnected. Besides, it can be observed in the Fig 8 (d) that all the inverter voltage amplitudes are constrained between $\pm 5\%$ of its nominal value. Lastly, it is worth noting that the execution time of the proposed MPC is 5 μs.

Additionally, in order to validate the robustness against the line impedance ratio, the designed MPC has been tested with the mainly resistive inverters, disconnecting the inverters 1 and 2. Besides, the controller response under a sudden load change is studied with a mainly resistive microgrid. Fig. 9 shows the inverters active and reactive power, their frequencies

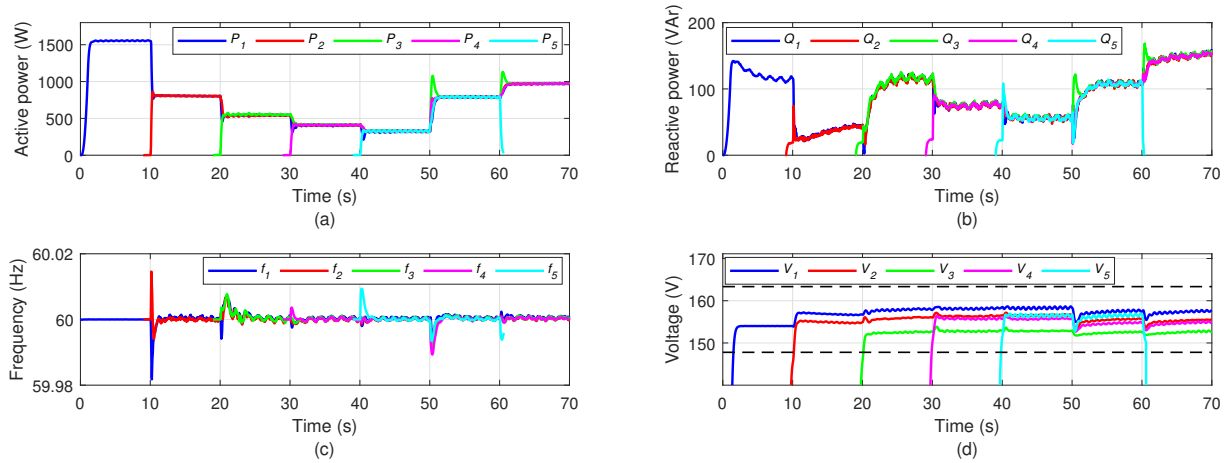

Fig. 8. Performance evaluation of the proposed controller: (a) active power, (b) reactive power, (c) frequencies, and (d) bus voltage.

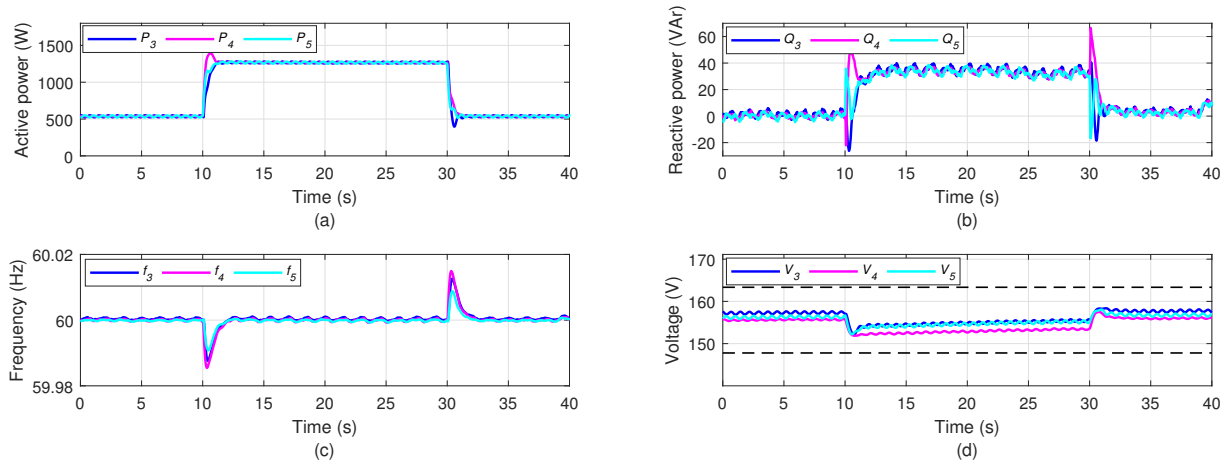

Fig. 9. Performance evaluation of the proposed controller with a resistive line impedance scenario

and the bus voltages. It should be noted that any impedance configuration not compromise the steady-state performance of the proposed control. Besides, it should be noted that since the microgrid line impedance is mainly resistive, the reactive power with low power demand it almost zero.

Furthermore, to validate the performance of the proposed control scheme under non-ideal conditions, e.g. communication failures, unbalanced and nonlinear load, the proposed controller will be compared with a distributed droop-inspired control (droop-free) [13]. The droop-free control parameters have been designed to obtain similar dynamics among the proposed control. Moreover, to yield stability and increase the accurate power sharing, the droop-free control needs a virtual impedance [17]. The following subsections show the comparison between the proposed MPC and the droop-free control in non ideal scenarios.

B. Non ideal Communication Study

The distributed control system relies on the availability of communications. Besides, in large distributed systems the units may be far away, thus the communication services may be affected, e.g. communication link failures, transmission delay, data losses, etc. Therefore, the system performance may be compromised. To evaluate the performance of the proposed MPC under nonideal communication parameters, two different tests were designed.

In the first experiment, the controllers have been tested under a sudden load change with a transmission rate of 0.5 s. Fig. 10 shows the transient active and reactive power in response to the step load change of the droop-free (a) and the proposed control (b). It should be noted that the steady-state is not compromised by the high transmission rate.

In the second experiment, the controllers also have been tested under a communication link failure and message losses (i.e. the probability that a message is lost during transmission). For this purpose the following experimental test was designed. At the time t = 0 s the five inverters were previously working with the original communication graph feeding a three-phase load, with a total power demand of 1.6 kW. Then, at time t = 5 s the communication link 4-5 has been disabled (i.e., a_{45} = 0). Besides, for each policy, the message losses are around 25 % and the transmission rate 0.1 s. Finally, at t = 10 s the second load is connected. Fig. 11 shows the active and reactive power under the described scenario. Fig. 11 (a) shows an inaccurate reactive power sharing using the droop-free control, when the link failure occurs and when the message losses is around 25

This article has been accepted for publication in a future issue of this journal, but has not been fully edited. Content may change prior to final publication. Citation information: DOI 10.1109/TIE.2021.3097608, IEEE Transactions on Industrial Electronics

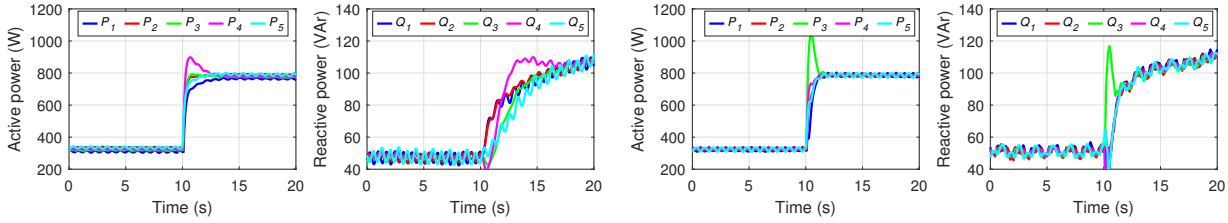

(a) (b)

Fig. 10. Performance of the distributed controllers with a transmission rate of 0.5 s: (a) droop-free [13], (b) proposed MPC.

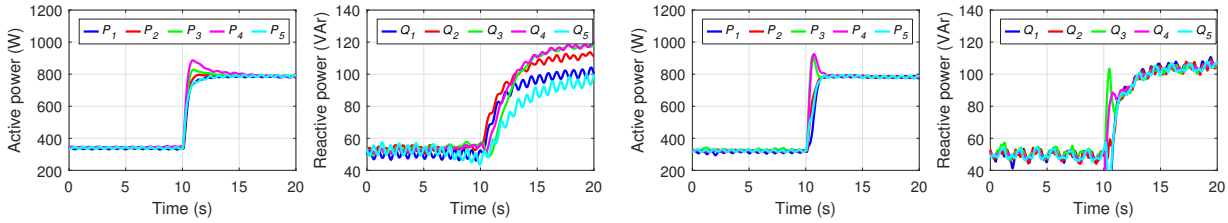

(a) (b)

Fig. 11. Performance of the distributed controllers during a failure in the communication link 4-5 and with 25% of losses in message transmissions: (a) droop-free [13], (b) proposed MPC.

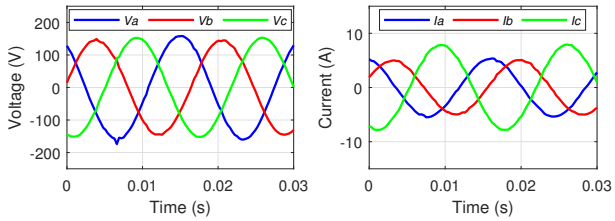

Fig. 12. Inverter 1 currents and voltages of the droop-free [13] under unbalanced load.

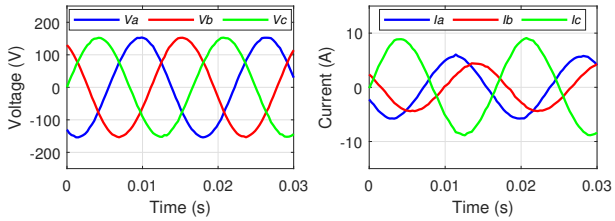

Fig. 13. Inverter 1 currents and voltages of the proposed control scheme under unbalanced load.

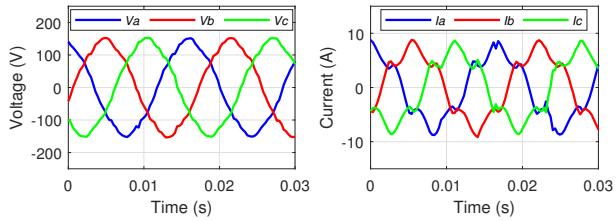

Fig. 14. Inverter 1 currents and voltages of the droop-free [13] under nonlinear load.

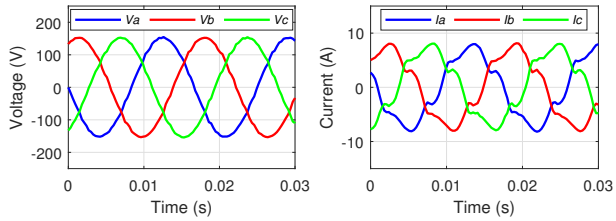

Fig. 15. Inverter 1 currents and voltages of the proposed control scheme under nonlinear load.

%. On the other hand, from Fig. 11 (b) it should be noted that the steady-state performance has not been affected by the communication failure and message losses using the proposed MPC. To sum up, the proposed control is resilient to a link communication failure.

C. Three-Phase Unbalanced Load Study

In this subsection, the controllers have been tested under a three-phase unbalanced load. The experiments have the following pattern. The inverter 1 and 2 are connected and feeding a three-phase balanced load connected in the bus, meanwhile, the inverter 3, 4 and 5 are disconnected. At the time t =0 s an unbalanced load is connected as a local load of inverter 1. Fig. 12 shows the inverter 1 voltage and current waveforms using the droop-free controller. Since the droop-free uses a virtual impedance with the output current as a feedforward term to generate the voltage references. Hence, the voltage waveforms are unbalanced. The same waveforms are shown in Fig. 13 but using the proposed control. Since the proposed control does not need the virtual impedance term, the voltage waveforms are balanced although a unbalanced load is connected.

D. Nonlinear Load Study

Finally, the controllers have been tested in the presence of nonlinear loads. The following experiment has been designed. The inverter 1 and 2 are connected and feeding a three-phase balanced load connected to the bus, meanwhile, the inverter 3,

4 and 5 are disconnected. At the time t =0 s a nonlinear load is connected as a local load of inverter 1. Fig. 14-15 shows the performance of the droop-free and proposed controller under nonlinear loads, respectively. Fig. 14 shows the inverter 1 voltage and current waveforms using the droop-free controller. It should be noted that the current waveforms are distorted, and THD of the inverters 1 and 2 are 24.3% and 15.1%, respectively. Moreover, in both inverters 1 and 2, the voltage waveforms are distorted with a THD equal to 7.2% and 4.1%, respectively. The same waveforms are shown in Fig. 15 using the proposed controller. It should be noted that the current waveforms are distorted, and THD is equal to 22.1% and 10.2% for inverter 1 and 2, respectively, meanwhile in both inverters 1 and 2, the voltage waveforms have a sinusoidal form when the nonlinear load is connected. Moreover, the THD of the voltage inverter 1 and 2 are 1.5% and 1.2% respectively.

VII. Conclusions

In this paper, a novel large-signal model for grid-forming inverters connected to a microgrid based on the active and reactive power dynamic equations is proposed. This model allows to design a novel control scheme for AC microgrids. This controller uses the presented large-signal model with an embedded integrator to achieve a zero steady-state error in active and reactive power sharing, and robustness against any kind of line impedance without virtual impedance needed. Experimental results show that the proposed control provides a precise frequency and voltage regulation, regardless of the line impedance configuration. Besides, the experimental results show that the proposed control is resilient to communication single link failures. The experimental results have also shown that the proposed controller improves the power quality in the voltage and current waveforms provided by the inverters by reducing the THD, especially in unbalanced and nonlinear loads. As an open topic for future research, the application of new control schemes using the novel large-signal model in microgrids can be studied.

References

[1] R. H. Lasseter, "Certs microgrid," in *2007 IEEE Int. Conf. Syst. Eng.*, 2007, pp. 1–5.

[2] J. M. Guerrero, J. C. Vasquez, J. Matas, L. García de Vicuna, and M. Castilla, "Hierarchical control of droop-controlled AC and DC microgrids. A general approach towards standardization," *IEEE Trans. Ind. Electron.*, vol. 58, no. 1, pp. 158–172, Jan. 2011.

[3] J. Rocabert, A. Luna, F. Blaabjerg, and P. Rodríguez, "Control of power converters in ac microgrids," *IEEE Trans. on Power Electron.*, vol. 27, no. 11, pp. 4734–4749, 2012.

[4] D. E. Olivares, A. Mehrizi-Sani, A. H. Etemadi, C. A. Cañizares, R. Iravani, M. Kazerani, A. H. Hajimiragha, O. Gomis-Bellmunt, M. Saeedifard, R. Palma-Behnke, G. A. Jiménez-Estévez, and N. D. Hatziargyriou, "Trends in microgrid control," *IEEE Trans. on Smart Grid*, vol. 5, no. 4, pp. 1905–1919, 2014.

[5] Y. Han, H. Li, P. Shen, E. A. A. Coelho, and J. M. Guerrero, "Review of active and reactive power sharing strategies in hierarchical controlled microgrids," *IEEE Trans. on Power Electron.*, vol. 32, no. 3, pp. 2427–2451, 2017.

[6] J. M. Guerrero, J. Matas, L. Garcia De Vicuna, M. Castilla, and J. Miret, "Wireless-control strategy for parallel operation of distributed-generation inverters," *IEEE Transactions on Ind. Electron.*, vol. 53, no. 5, pp. 1461–1470, 2006.

[7] R. Majumder, A. Ghosh, G. Ledwich, and F. Zare, "Angle droop versus frequency droop in a voltage source converter based autonomous microgrid," in *2009 IEEE Power Energy Society General Meeting*, 2009, pp. 1–8.

[8] E. Rokrok and M. E. H. Golshan, "Adaptive voltage droop scheme for voltage source converters in an islanded multibus microgrid," *IET Gen. Trans. Distr.*, vol. 4, no. 5, pp. 562–578, 2010.

[9] K. Lao, W. Deng, J. Sheng, and N. Dai, "Pq-coupling strategy for droop control in grid-connected capacitive-coupled inverter," *IEEE Access*, vol. 7, pp. 31 663–31 671, 2019.

[10] H. Han, X. Hou, J. Yang, J. Wu, M. Su, and J. M. Guerrero, "Review of power sharing control strategies for islanding operation of ac microgrids," *IEEE Trans. on Smart Grid*, vol. 7, no. 1, pp. 200–215, 2016.

[11] J. M. Guerrero, M. Chandorkar, T. Lee, and P. C. Loh, "Advanced control architectures for intelligent microgrids—part i: Decentralized and hierarchical control," *IEEE Trans. on Ind. Electron.*, vol. 60, no. 4, pp. 1254–1262, 2013.

[12] J. M. Guerrero, P. C. Loh, T. Lee, and M. Chandorkar, "Advanced control architectures for intelligent microgrids—part ii: Power quality, energy storage, and ac/dc microgrids," *IEEE Trans. on Ind. Electron.*, vol. 60, no. 4, pp. 1263–1270, 2013.

[13] V. Nasirian, Q. Shafiee, J. M. Guerrero, F. L. Lewis, and A. Davoudi, "Droop-free distributed control for ac microgrids," *IEEE Trans. on Power Electron.*, vol. 31, no. 2, pp. 1600–1617, 2016.

[14] J. Schiffer, T. Seel, J. Raisch, and T. Sezi, "Voltage stability and reactive power sharing in inverter-based microgrids with consensus-based distributed voltage control," *IEEE Transactions on Control Systems Technology*, vol. 24, no. 1, pp. 96–109, 2016.

[15] S. M. Mohiuddin and J. Qi, "Droop-free distributed control for ac microgrids with precisely regulated voltage variance and admissible voltage profile guarantees," *IEEE Transactions on Smart Grid*, vol. 11, no. 3, pp. 1956–1967, 2020.

[16] D. K. Dheer, O. V. Kulkarni, S. Doolla, and A. K. Rathore, "Effect of reconfiguration and meshed networks on the small-signal stability margin of droop-based islanded microgrids," *IEEE Trans. on Ind. Applic.*, vol. 54, no. 3, pp. 2821–2833, 2018.

[17] J. He and Y. W. Li, "Analysis, design, and implementation of virtual impedance for power electronics interfaced distributed generation," *IEEE Trans. on Ind. Applic.*, vol. 47, no. 6, pp. 2525–2538, 2011.

[18] A. Trivedi and M. Singh, "l_1 adaptive droop control for ac microgrid with small mesh network," *IEEE Trans. on Ind. Electron.*, vol. 65, no. 6, pp. 4781–4789, 2018.

[19] E. A. A. Coelho, P. C. Cortizo, and P. F. D. Garcia, "Small signal stability for single phase inverter connected to stiff ac system," in *Conference Record of the 1999 IEEE Ind. Applic. Conference. Thirty-Forth IAS Annual Meeting (Cat. No.99CH36370)*, vol. 4, 1999, pp. 2180–2187 vol.4.

[20] X. Guo, Z. Lu, B. Wang, X. Sun, L. Wang, and J. M. Guerrero, "Dynamic phasors-based modeling and stability analysis of droop-controlled inverters for microgrid applications," *IEEE Trans. on Smart Grid*, vol. 5, no. 6, pp. 2980–2987, 2014.

[21] M. Farrokhabadi, C. A. Cañizares, J. W. Simpson-Porco, E. Nasr, L. Fan, P. A. Mendoza-Araya, R. Tonkoski, U. Tamrakar, N. Hatziargyriou, D. Lagos, R. W. Wies, M. Paolone, M. Liserre, L. Meegahapola, M. Kabalan, A. H. Hajimiragha, D. Peralta, M. A. Elizondo, K. P. Schneider, F. K. Tuffner, and J. Reilly, "Microgrid stability definitions, analysis, and examples," *IEEE Trans. on Power Systems*, vol. 35, no. 1, pp. 13–29, 2020.

[22] L. Wang, *Model Predictive Control System Design and Implementation Using MATLAB*. Springer, 2009.

[23] R. Guzman, L. G. de Vicuña, A. Camacho, J. Miret, and J. M. Rey, "Receding-horizon model-predictive control for a three-phase vsi with an lcl filter," *IEEE Trans. Ind. Electron.*, vol. 66, no. 9, pp. 6671–6680, Sep. 2019.

[24] R. Perez-Ibacache, A. Cedeno, C. Silva, G. Carvajal, J. Aguero, and A. Yazdani, "Decentralized model-based predictive control for der units integration in ac microgrids subject to operational and safety constraints," *IEEE Transactions on Power Delivery*, pp. 1–1, 2020.

[25] C. Zheng, T. Dragicevic, and F. Blaabjerg, "Model predictive control based virtual inertia emulator for an islanded ac microgrid," *IEEE Transactions on Industrial Electronics*, pp. 1–1, 2020.

[26] Z. Zhao, J. Zhang, B. Yan, R. Cheng, C. S. Lai, L. Huang, Q. Guan, and L. L. Lai, "Decentralized finite control set model predictive control strategy of microgrids for unbalanced and harmonic power management," *IEEE Access*, vol. 8, pp. 202 298–202 311, 2020.

[27] Y. Shan, J. Hu, Z. Li, and J. M. Guerrero, "A model predictive control for renewable energy based ac microgrids without any pid regulators,"

IEEE Transactions on Power Electronics, vol. 33, no. 11, pp. 9122–9126, 2018.

[28] T. Chen, O. Abdel-Rahim, F. Peng, and H. Wang, "An improved finite control set-mpc-based power sharing control strategy for islanded ac microgrids," *IEEE Access*, vol. 8, pp. 52 676–52 686, 2020.

[29] A. Saleh, A. Deihimi, and R. Iravani, "Model predictive control of distributed generations with feed-forward output currents," *IEEE Trans. on Smart Grid*, vol. 10, no. 2, pp. 1488–1500, March 2019.

[30] G. Lou, W. Gu, W. Sheng, X. Song, and F. Gao, "Distributed model predictive secondary voltage control of islanded microgrids with feedback linearization," *IEEE Access*, vol. 6, pp. 50 169–50 178, 2018.

[31] G. Lou, W. Gu, Y. Xu, M. Cheng, and W. Liu, "Distributed mpc-based secondary voltage control scheme for autonomous droop-controlled microgrids," *IEEE Transactions on Sustainable Energy*, vol. 8, no. 2, pp. 792–804, 2017.

[32] C. Ahumada, R. Cárdenas, D. Sáez, and J. M. Guerrero, "Secondary control strategies for frequency restoration in islanded microgrids with consideration of communication delays," *IEEE Transactions on Smart Grid*, vol. 7, no. 3, pp. 1430–1441, 2016.

[33] H. Markiewicz and A. Klajn, "Voltage disturbances standard en 50160 - voltage characteristics in public distribution systems," 2008.

[34] W.-H. Chen, "Stability analysis of classic finite horizon model predictive control," *International Journal of Control, Automation and Systems*, vol. 8, no. 2, pp. 187–197, April 2010.

Carlos Alfaro was born in San Salvador, El Salvador. He received the B.S. in mechanical engineering from the Universidad Centroamericana "José Simeón Cañas" (UCA), El Salvador, in 2015, and M.S. in automatic systems and industrial electronics engineering from the Technical University of Catalonia, Spain, in 2018. He is currently working toward the Ph.D. degree in the Department of Electronic Engineering, Technical University of Catalonia. His current research interests include power electronics, nonlinear and predictive control.

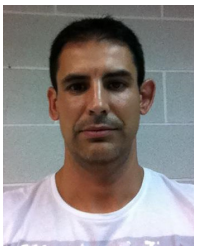

Ramon Guzman received the B.S., the M.S. and the Ph.D. degrees in telecommunications engineering from the Technical University of Catalonia, Barcelona, Spain, in 1999, 2004 and 2016, respectively. He is currently an Associate Professor with the Department of Automatic Control in the Technical University of Catalonia. His research interests include nonlinear and adaptive control for three-phase power converters. Ramon Guzman is a member of the IEEE Industrial Electronics Society and becomes to the Renewable Energy Systems Subcommittee of Power Electronics Technical Committee of IES. Dr. Guzman is an Associate Editor of the IEEE Transactions on Industrial Electronics.

Luis Garcia de Vicuña received the Ingeniero de Telecomunicación and Dr.Ing. degrees from the Technical University of Catalonia, Barcelona, Spain, in 1980 and 1990, respectively, and the Dr.Sci. degree from the Université Paul Sabatier, Toulouse, France, in 1992. He is currently a Full Professor in the Department of Electronic Engineering, Technical University of Catalonia, where he teaches courses on power electronics. His research interests include power electronics modeling, simulation and control, active power filtering, and high-power-factor ac/dc conversion.

Jaume Miret (M'98) received the B.S. degree in telecommunications, M.S. degree in electronics, and Ph.D. degree in electronics from the Universitat Politecnica de Catalunya, Barcelona, Spain, in 1992, 1999, and 2005, respectively. From 1993 to 2011, he was an Assistant Professor in the Department of Electronic Engineering, Universitat Politecnica de Catalunya, Spain. Since 2011 he has been an Associate Professor in the Universitat Politecnica de Catalunya. His research interests include dc-to-ac converters, active power filters, and digital control.

Miguel Castilla received the B.S., M.S., and Ph.D. degrees in telecommunication engineering from the Technical University of Catalonia, Barcelona, Spain, in 1988, 1995, and 1998, respectively. Since 2019, he has been a Full Professor with the Department of Electronic Engineering, Technical University of Catalonia, where he teaches courses on control of power electronic converters. His research interests include the areas of power electronics, control, renewable energy systems, and electrical microgrids.